Structural and optical properties of visible active photocatalytic WO_3 thin films prepared by reactive dc magnetron sputtering

Malin B. Johansson,[a] Gunnar A. Niklasson, and Lars Österlund[b]
Department of Engineering Sciences, The Ångström Laboratory, Uppsala University, SE-751 21 Uppsala, Sweden

(Received 27 June 2012; accepted 22 October 2012)

Nanostructured tungsten trioxide films were prepared by reactive dc magnetron sputtering at different working pressures P_{tot} = 1–4 Pa. The films were characterized by scanning electron microscopy, x-ray diffraction, Rutherford backscattering spectroscopy, Raman spectroscopy, and ultraviolet–visible spectrophotometry. The films were found to exhibit predominantly monoclinic structures and have similar band gap, $E_g \approx 2.8$ eV, with a pronounced Urbach tail extending down to 2.5 eV. At low P_{tot}, strained film structures formed, which were slightly reduced and showed polaron absorption in the near-infrared region. The photodegradation rate of stearic acid was found to correlate with the stoichiometry and polaron absorption. This is explained by a recombination mechanism, whereby photoexcited electron–hole pairs recombine with polaron states in the band gap. The quantum yield decreased by 50% for photon energies close to E_g due to photoexcitations to band gap states lying below the O_2 affinity level.

I. INTRODUCTION

Research on photocatalytic (PC) materials has attracted much interest as a sustainable method for pollutant degradation, water splitting, and synthetic fuel production.[1–3] Nanocrystalline forms of wide band gap semiconducting oxides, and primarily, the anatase form of TiO_2, is by far the most studied of these materials.[1,4] TiO_2 requires, however, ultraviolet (UV) light to excite the chemically active valence electrons to the conduction band, and solar-based conversion is thus limited to ~4% of the sunlight. Since it is desirable to exploit also visible light, a second generation of efficient UV–visible active PC materials is currently sought, where, e.g., low-dimensional doped TiO_2, WO_3, and mixed metal oxides, with and without additions of noble metals for enhanced electron–hole pair separation, have received considerable attention.[5–8] WO_3 is a promising material for a wide range of environmental and energy applications. The electrochromic effect of WO_3 has been widely studied, and the material is much used in fabrication of smart windows.[9–11] PC oxidation for indoor air purification and self-cleaning is today considered in several applications in the built environment.[12,13] Recently, WO_3 has drawn attention because of its high efficiency in PC activity under daylight illumination[14–17] and its ability to photodegrade a wide range of environmental pollutants.[16,18,19] Nano-WO_3 is reported to have much higher PC activity compared to bulk WO_3 photoelectrodes.[5,20] This is related to the different mechanism of charge separation and charge transport in the nanocrystalline semiconductor films, which is a subject of continuing discussion.[21]

The PC activity depends on the electronic structure, which is related to crystal structure and surface morphology. WO_3 exists in several phases, which differ with respect to each other by the tilting and displacement of the atoms in the octahedral building blocks that comprise the WO_3 structure. The thermodynamically favored phase is reported to change with temperature (at standard pressure) for crystalline bulk WO_3 as follows: monoclinic *Pc* (ε-WO_3) up to 230 K, triclinic *P*1 (δ-WO_3) 230–300 K, monoclinic $P2_1/n$ (γ-WO_3) 300–623 K, orthorhombic *Pnma* (β-WO_3) 623–1020 K, tetragonal *P*4/*ncc* (α-WO_3) 1020–1171 K, and, finally, tetragonal *P*4/*nmm* (α-WO_3) to the melting point at 1700 K.[22–26] The stability of each of these phases is modified by preparation procedures. For nanocrystalline thin films, the detailed growth conditions are critical, including type of substrate, temperature, and pressure. Apart from high surface area, which is beneficial in many environmental applications, nano-WO_3 exhibits structures and morphologies with unique properties that do not exist in bulk. The small size of grains in a material can substantially influence charge transport, electronic band structure, and optical properties. Nano-WO_3 is readily reduced, and nonstoichiometry is reported to involve structural changes.[27–29] Substoichiometry gives rise to polarons, which change the optical properties and increase the absorption in the near-infrared (NIR) spectral region.[29,30] For small values of substoichiometry, x, crystals of WO_{3-x} are reported to undergo a structural phase transition from the room temperature δ phase to the low temperature ε phase at $T \sim 250$ K.[31] The δ phase shows metallic behavior, and the ε phase has insulating properties for the electron/hole carriers.[32] Reported values for the electronic band gap of

Address all correspondence to these authors.
[a]e-mail: malin.johansson@angstrom.uu.se
[b]e-mail: lars.osterlund@angstrom.uu.se
DOI: 10.1557/jmr.2012.384

 © Materials Research Society 2012

https://doi.org/10.1557/jmr.2012.384 Published online by Cambridge University Press

nano-WO_3 vary considerably from $E_g = 2.6$ to 3.25 eV,[33,34] and this is probably due to a combination of one or several of the effects discussed above. Further, the small size of nano-WO_3 crystallites will enhance the surface energy of the system.[35,36] With higher surface energy, the melting point and temperature for phase transitions decrease.[37]

In this article, we report on the preparation and characterization of the structural, optical, and PC properties of nano-WO_3 films made with reactive dc magnetron sputtering. This method offers freedom in deposition conditions and is suitable to span a large parameter space to address some of the issues discussed above. In particular, the physical properties of nano-WO_3 films have been studied as a function of working pressure, P_{tot}. The photodegradation of stearic acid (SA) was measured to determine the degradation rate and quantum yield for the different nano-WO_3 films prepared at different P_{tot}.

II. EXPERIMENTAL SECTION

A. Sample preparation

Nanocrystalline tungsten oxide thin films were prepared by reactive dc magnetron sputtering using a versatile deposition system based on a Balzers UTT 400 unit (Balzers AG, Balzers, Liechtenstein). The sputter target was a 5-cm-diameter plate of W with 99.95% purity (Plasmaterials, Inc., Livermore, CA). Sputtering was conducted in a plasma of Ar and O_2. The purity of the gases was 99.998%, and the sputtering power was set to 200 W with the substrates positioned 13 cm from the target. The total working pressure was varied between $P_{tot} = 1.3$, 2.0, 3.3, and 4.0 Pa, respectively. The substrate temperature was maintained at $T_s = 553$ K, and the O_2/Ar gas flow ratio was kept fix at 0.43. The deposition time was set at 35 min, and the sample holder was rotating with constant speed to obtain uniform thickness of the films. The samples were subsequently postannealed at $T_a = 673$ K for 1 h. Films were sputtered on 13-mm-diameter CaF_2 substrates (Crystran Ltd., Poole, UK). The CaF_2 substrates were cleaned with deionized water and ethanol before sputtering.

B. Material characterization

The surface morphology and grain sizes of the formed nanostructures were characterized with scanning electron microscopy (SEM), using a LEO 1550 FEG instrument (LEO Electron Microscopy Ltd., Cambridge, UK) with in-lens detector operating at 10 kV.

The crystalline structure of the films was determined by x-ray diffraction (XRD). For thin films, grazing incidence x-ray diffraction (GIXRD) was used (Siemens D5000 Th-2Th, PANalytical B.V., Almelo, Netherlands), using Cu K_α ($\lambda = 1.54051$ Å) radiation. Scans were taken in the range from 10 to 90° (2θ). Broadening of the diffraction peaks due to the average grain size, L, and strain, ε, are present simultaneously and were extracted from experimental data using the Williamson–Hall method[38]:

$$\cos(\theta)(\beta_c - \beta_i) = \frac{k\lambda}{L} + \langle \varepsilon^2 \rangle^{1/2} \sin(\theta) \quad , \qquad (1)$$

where $\varepsilon = \Delta L/L$ is the strain in the [hkl] direction, $k \approx 0.9$ is the geometric shape factor for a spherical scatterer, λ is the x-ray wave length, β_c the full width at half maximum, FWHM, of the XRD peak, β_i the instrumental broadening, and θ the diffraction angle. The program XPERT PRO was used to remove the contribution from the Cu $K_{\alpha 2}$ line and determine β_c. Peaks in the diffractograms were fitted to a weighted superposition of the Gauss and Cauchy functions.

Raman spectra were recorded in backscattering geometry using a confocal Raman microscope (HR800 Labram; Horiba Jobin-Yvon, Lille, France). A 514-nm Ar laser was directed through a 50x long working distance objective (NA = 0.45), using a 600 grooves/mm grating, yielding a spectral resolution of approximately 3.5 cm^{-1}. A low laser power (5 mW) was used to ensure that no structural modifications of the samples occurred due to local laser heating. The spectra were calibrated against the Si peak at 520.7 cm^{-1} of a Si(110) wafer.

Composition, stoichiometry, and density were determined using the Rutherford backscattering spectroscopy (RBS) on films deposited on C substrates. The measurements were carried out at the Uppsala Tandem Accelerator Laboratory using ^{4}He ions at energy of 2 MeV. An azimuthal angle $\alpha = 7°$ was applied to avoid the risk of channeling into the crystals. The ions were backscattered at an angle of 172°. Data were analyzed with the program SIMNRA, which yielded the number of atoms per cm^2 (N_s) and the number of atoms in a formula unit (N). For a perfect stoichiometric film, the number of atoms in a WO_3 unit is $N = 4$, and for understoichiometric films, $N = 4 - X$, where X is the number of missing O atoms. Film density, δ, was calculated from the formula:

$$\rho = \frac{MN_s}{NdN_A} \quad , \qquad (2)$$

where M is the mass per mol of formula unit, N_A is the Avogadro constant, and d is the film thickness (in cm).

Optical properties were measured with a Perkin-Elmer Lambda 900 double-beam UV/Vis/NIR spectrophotometer (PerkinElmer, Waltham, MA) equipped with an integrating sphere and a Spectralon reflectance standard. The absorptance, $A(\lambda)$, was determined from measured transmittance, $T(\lambda)$, and reflectance, $R(\lambda)$, according to:

$$A(\lambda) = 1 - T(\lambda) - R(\lambda) \quad , \qquad (3)$$

and using appropriate corrections for diffuse scattering and instrument calibration.[39]

The film thickness, d, was determined both from surface profilometry (Tencor Alpha Step 200, SPEC,

https://doi.org/10.1557/jmr.2012.384 Published online by Cambridge University Press

Santa Clara, CA) and calculated from the interference fringes seen in optical transmittance data, following the method of Swanepoel[40]:

$$d = \frac{\lambda_1 \lambda_2}{2(\lambda_1 n_2 - \lambda_2 n_1)} \quad , \tag{4}$$

where n_1 and n_2 are the refractive indices at two adjacent transmittance maxima at λ_1 and λ_2, respectively. The refractive index of the of CaF_2 substrate, s, was determined from transmittance measurements of the bare substrate. From the transmittance maxima, T_M, and minima, T_m, of the interference fringes seen in the spectrum for WO_3 thin films on CaF_2 substrates, a refraction number, N, was calculated according to:

$$N = 2s\frac{T_M - T_m}{T_M T_m} + \frac{s^2 + 1}{2} \quad . \tag{5}$$

The refractive index, n, of the films was then calculated from the equation:

$$n = [N + (N^2 - s^2)^{1/2}]^{1/2} \quad . \tag{6}$$

From $T(\lambda)$ and $R(\lambda)$, the absorption coefficient, $\alpha(\lambda)$, can be determined according to[41]:

$$\alpha(\lambda) = \frac{1}{d}\ln\left(\frac{1 - R(\lambda)}{T(\lambda)}\right) \quad , \tag{7}$$

where d is the thickness of the film.

C. Photodegradation measurements

Photodegradation of SA ($C_{18}H_{36}O_2$; Merck, Darmstadt, Germany) was measured with Fourier transform infrared (FTIR) spectroscopy operated in transmission mode using a Bruker IFS66v/S spectrometer (Bruker, AZ Wormer, Netherlands). FTIR spectra were recorded with 4 cm^{-1} resolution using 30 s scan time per spectrum and 30 s dwell time between consecutive spectra. Application of SA was done following earlier reported methods to determine self-cleaning properties of TiO_2.[42,43] SA was applied to the surface of the WO_3 films by pipetting 10 mm^3 of 0.8 mM methanol solution followed by spin coating at 1500 rpm. FTIR spectra were, after appropriate baseline corrections, integrated between 2700 and 3000 cm^{-1}, which contains the ν(C–H) vibrations in SA. The number of SA molecules per cm^2 per integrated absorbance unit (1 A.U.) in this wave number region has previously been reported to be $N_{1A.U.} = 3.17 \times 10^{15}$ molecules/cm^2 for TiO_2.[42] The number of SA adsorption sites on the WO_3 surface were estimated using an organic dye molecule D35 ($C_{54}H_{58}N_2O_6S$; Merck; M_w = 863.11 g/mol) as previously reported.[44] D35 has one anchoring carboxyl group just like SA. A sample of WO_3 thin film was immersed for 12 h in 0.2 mM solution of dye dissolved in ethanol. Absorbance spectra were measured using a Perkin-Elmer Lambda 900 double-beam UV/Vis/NIR spectrophotometer. The absorbance of the bare WO_3 thin film on a CaF_2 substrate was subtracted to obtain the absorbance due to D35. To calibrate the absorbance, a dye solution of 0.01 mM in ethanol was recorded on a HR-2000 Ocean Optics fiber optics spectrophotometer (Ocean Optics, Dunedin, FL). A normal quartz cuvette (1 cm path length) was used for the measurement of dye solution. From the Beer–Lambert's law, $I = I_0 \times 10^{-\varepsilon c d}$, where ε is the extinction coefficient (ε_{D35} = 31300 M^{-1}/cm), c the concentration, and d the thickness, the D35 concentration on the WO_3 film was determined to 0.0013 mM, which corresponds to 0.0013 μmol/cm^2 or 7.82×10^{14} molecules/cm^2.

A Hg arc lamp operated at 300 W was used as irradiation source. Band-pass filters (Oriel Instruments, Stratford, CT) centered at 546, 436, 406, and 313 nm, respectively, each with a bandwidth of $\Delta\lambda = 10$ nm, were used to measure the photodegradation rate at different wave lengths in the band gap region. To reduce the infrared part of the lamp spectrum, the light was first directed through a 75-mm-long water filter (Milli-Q water, 18.2 MΩ). The light was collected into a fused silica fiber bundle and directed onto the sample cell through a CaF_2 window at an angle of 25° to the surface normal. The photon power was measured to be 102 mW/cm^2 in the spectral range between 300 and 800 nm using a thermopile detector (Ophir, North Andover, MA).

A lower limit of the quantum yield, Φ (assuming all absorbed photons in the film reach the surface), was calculated according to:

$$\Phi = \frac{N_{1A.U.} A_0 k_{dec}}{\int F(\lambda)(1 - e^{-\alpha(\lambda)d})d\lambda} \quad , \tag{8}$$

where A_0 is the integrated absorbance between 2700 and 3000 cm^{-1} due to SA at $t = 0$ min, k_{dec} is the degradation rate (s^{-1}), $F(\lambda)$ is the photon flux (s^{-1}/cm^2), $(1 - e^{-\alpha(\lambda)d})$ is the absorption in the WO_3 film, and d is the film thickness.

In a second experiment, simulated solar light was used using a Xe arc lamp source operated at 200 W and filtered through a set of air mass filters (AM1.5). The light source setup was otherwise identical to the one described above. The photon power was measured to be 100 mW/cm^2 in the wave length range 300–800 nm in these experiments.

III. RESULTS AND DISCUSSION

A series of WO_3 thin films were prepared by reactive dc magnetron sputtering at different working pressures (Table I). All samples showed high optical transparency after postannealing at T_a = 673 K for 1 h. The samples sputtered at low working pressure, P_{tot} = 1.3 and 2.0 Pa,

https://doi.org/10.1557/jmr.2012.384 Published online by Cambridge University Press

showed a light bluish color, whereas films prepared at $P_{tot} = 3.3$ and 4.0 Pa showed a slight yellow to red coloring.

A. Scanning electron microscopy

Figure 1 shows SEM images of sputtered nano-WO_3 films prepared at low and high P_{tot}, respectively. It is evident from Fig. 1(a) that films with rectangular shaped structures are formed at low P_{tot}. Inspection of the images reveals that sizes of these structures are approximately between 30 and 60 nm. At $P_{tot} = 4.0$ Pa, the films appear to consist of structures with rounder shapes [Fig. 1(b)]. The underlying substrate is clearly seen in the cracks between the structures, which is consistent with lower deposition rate with increasing P_{tot} and hence thinner films. The image indicates a relatively porous morphology, where the grain boundaries are smeared out.

TABLE I. Summary of process parameters and physical properties of nano-WO_3 films fabricated by reactive dc magnetron sputtering.

Sample	Working pressure, P_{tot} (Pa)	Gas flow ratio O_2/Ar	Grain size[a] (nm)	Thickness[b] (nm)	Refractive[c] index, n	Density (g/cm^3)
a	1.3	0.43	15	1112	2.14	6.58
b	2.0	0.43	28	872	2.07	N/A
c	3.3	0.43	49	460	2.1	N/A
d	4.0	0.43	55	400	2.01	6.38

[a]From Eq. (1).
[b]From Eq. (4).
[c]From Eq. (6) at $\lambda = 550$ nm.

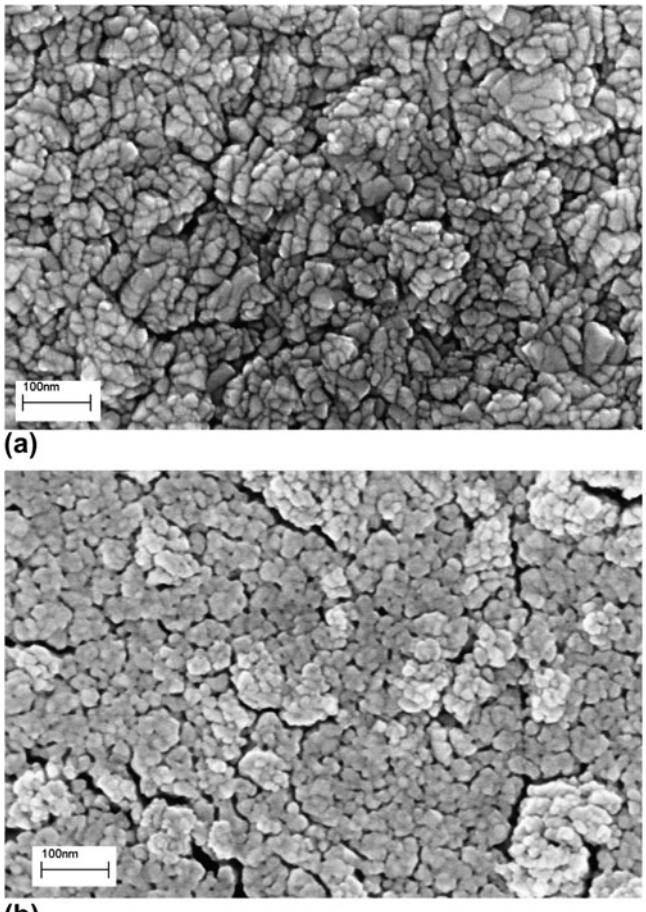


FIG. 1. SEM images of nano-WO_3 thin films sputtered at (a) $P_{tot} = 1.3$ Pa and (b) $P_{tot} = 4.0$ Pa. The films were sputtered at $T_s = 553$ K and postannealed at $T_a = 673$ K for 1 h.

B. Rutherford backscattering spectroscopy

Figure 2 shows spectra from RBS measurements of films prepared at low and high P_{tot}, respectively. Also shown in Fig. 2 are corresponding simulated spectra using SIMNRA, from which the stoichiometry and density of the films were obtained.[45] In all cases, the nano-WO_3 films exhibited a stoichiometry of WO_{3-x} with $|x| < 0.1$. However, within the uncertainty in these calculations (4%), the variation in x of nano-WO_3 films due to different P_{tot} could not be distinguished. The calculated density was determined to be $\delta = 6.58$ g/cm^3 and $\delta = 6.38$ g/cm^3 for films prepared at $P_{tot} = 1.3$ and 4.0 Pa, respectively. The RBS results show that high sputtering rates (i.e., low P_{tot}) result in more dense films, while low sputtering rates (i.e., high P_{tot}) result in films with lower density. Compared with the bulk density of WO_3 ($\delta = 7.14$ g/cm^3), it is seen that the film porosity is between 8% and 11%, i.e., the films are rather compact. These results qualitative corroborate the SEM results presented above.

C. X-ray diffraction

Figure 3 depicts XRD spectra of nano-WO_3 films at different P_{tot}. The structural distortions of the corner-sharing WO_6 octahedra comprising the WO_3 unit cell are quite complex and make definitive assignments of WO_3 phases from XRD data alone rather difficult, despite the apparent simple stoichiometry of WO_3. In Fig. 3, the most interesting part of the spectra, acquired between $2\theta = 10°$ and 90°, is extracted. The first diffraction peaks in Fig. 3 correspond to reflection from the (002), (020), and (200) planes, respectively, and are in good agreement with reported diffractograms for the δ-WO_3 and monoclinic γ-WO_3 phases.[46] These two phases are very similar with respect to angular distortions and atomic distances and are thus expected to have similar thermodynamic stability. Indeed, both phases have been reported to coexist at room temperature and are sensitive to the way the samples are prepared, e.g., T_s, T_a, and P_{tot}.[46–48] However, the (002) diffraction angle in ε-WO_3 at 23.19° is close to the corresponding reflections in the γ-WO_3 and δ-WO_3 phases,[29] which occur at 23.12°,[46] and the experimental value of the peak at 23.15° may indicate mixing of the low temperature monoclinic ε-WO_3 phase at low P_{tot}. Supporting this argument is the observation of the peak at 24.25°,

https://doi.org/10.1557/jmr.2012.384 Published online by Cambridge University Press

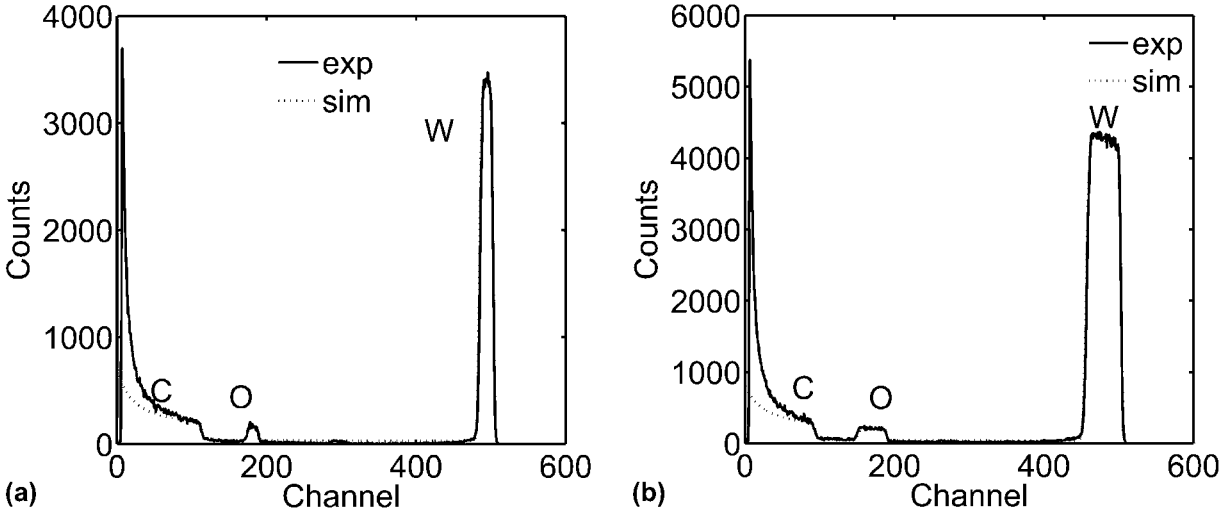


FIG. 2. RBS spectra of nano-WO_3 thin films on carbon substrates, sputtered at (a) P_{tot} = 1.3 Pa and (b) P_{tot} = 4.0 Pa, respectively.

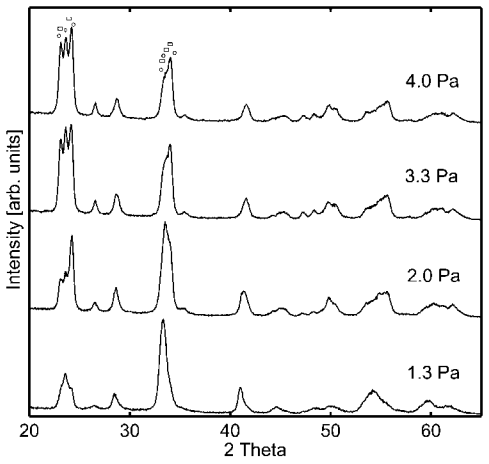


FIG. 3. XRD patterns of the nano-WO_3 thin films prepared at different P_{tot} = 1.3 – 4.0 Pa. Circles correspond to diffraction peaks due to γ-WO_3 [(from the left (002), (020), (200), (−202), (022) and (202)]. Squares correspond to diffraction peaks due to ε-WO_3 [(from the left (002), (110), (−112), (200) and (112)].

which is shifted to lower diffraction angles compared with references for the monoclinic γ-WO_3 (200) planes at 24.37° and triclinic δ-WO_3 (200) planes at 24.33°.[46] This may be due to a feature from the low temperature monoclinic phase ε-WO_3 (110) planes at 24.11°. Finally, it is apparent that the intensity of the peak corresponding to the (020) planes decreases relative to peaks from diffraction planes of (002) and (200) with increasing P_{tot}. In the range 2θ = 33–35°, the highest intensity occurs at P_{tot} = 1.3 Pa, and the diffractogram resembles the ε-WO_3 phase, which has an analogous XRD pattern, and a dominant peak at 33.34°, corresponding to the (−112) reflection,[29] again supporting significant ε-WO_3 phase mixing at low P_{tot}. With increasing P_{tot}, the relative intensity of the (−112) reflection decreases compared to the adjacent peak from diffraction planes of (202) at 34.08, which eventually dominates the XRD spectrum at P_{tot} = 4.0 Pa, and corresponds to reflection in either the δ-WO_3 or the γ-WO_3 phase, which is reported to occur at 34.08° and 34.17°, respectively. Which one of these latter two phases is most abundant cannot be determined from the XRD data. The phase transitions in nano-WO_3 films occur gradually rather than abruptly, as in bulk WO_3, and result in a range of coexisting phases depending on exact preparation conditions. However, previous reports have shown that the temperature range of coexisting δ and ε phases is much larger than the simultaneous existence of δ and γ phases,[46] which may indicate that the ε and δ phases are the dominant phases in our nano-WO_3 films.

In Fig. 3, it is seen that the intensity of the diffraction peaks in the 22.5–24.5° range increases with increasing P_{tot}, whereas the intensity of the peaks in the range 33–35° decreases. We conclude that the nano-WO_3 exhibits a preferred growth direction depending on P_{tot}, which changes with increasing pressure from the [202] and [−112] directions to the [020] and [200] directions.

Average grain size and strain were calculated from the broadening of the diffraction peaks using Eq. (1). Figure 4 shows a Williamson–Hall plot, where the experimental data are fitted by straight lines. The strain was obtained from the slope of the lines and the grain size from their intersection with the *y*-axis. It is seen that strain is significant for films sputtered at 1.3 Pa with ε ≈ 3.6%, while it is ε ≈ 1.7% for films sputtered at 4.0 Pa. The high strain in the film sputtered at 1.3 Pa is probably caused by imperfections such as oxygen vacancies, phase mixing with the ε-phase, and may also be related to its higher density. The average grain sizes are given in Table I. The linear fit is more uncertain for the sample prepared at 1.3 Pa due to overlapping reflection peaks, which are difficult to unambiguously separate.

https://doi.org/10.1557/jmr.2012.384 Published online by Cambridge University Press

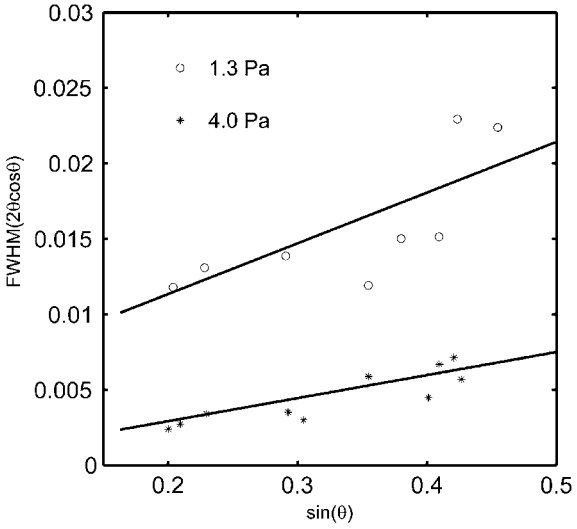


FIG. 4. Williamson–Hall plot using data on diffraction angle and broadening from experimental XRD spectra. Fits to Eq. (1) are given by the straight lines. The approximate linear relations indicate strain effects in films sputtered at 1.3 Pa, $\varepsilon = 3.6\%$ with average grain size $L = 15$ nm and at 4.0 Pa, $\varepsilon = 1.7\%$ and $L = 55$ nm.

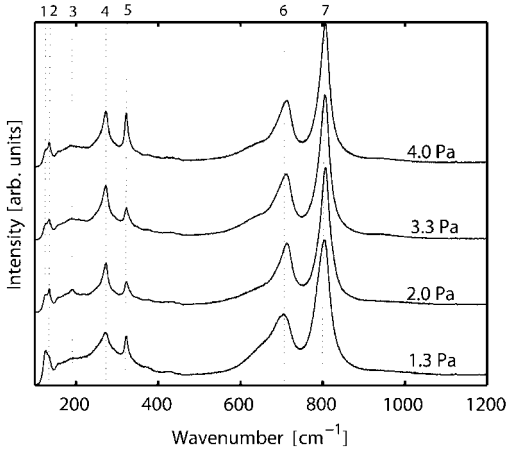


FIG. 5. Raman spectra of nano-WO_3 films prepared at different P_{tot}. Peaks are labeled **1** = 125 cm^{-1}, **2** = 136 cm^{-1}, **3** = 184 cm^{-1}, **4** = 274 cm^{-1}, **5** = 323 cm^{-1}, **6** = 715 cm^{-1}, and **7** = 807 cm^{-1}.

Low P_{tot} and hence high sputter rate, i.e., high kinetic energy of the particles bombarding the surface, may result in slight compression of the films, which is reported to influence the WO_3 structure and phase.[47] Under these sputter conditions, significant amounts of oxygen vacancies may also be created, which give rise to polarons (see below).[34] In nano-WO_3 thin films, both grain size and substrate interactions are suggested to change the relative thermodynamic stability of WO_3 phases.[37] A transition to a compressed phase can be obtained either by using high external pressure or by accumulating internal compressive strain due to polarons.[23,47] It has been reported that slightly reduced WO_{3-x}, with $x \approx 0.05$, promotes formation of the ε phase,[29] qualitatively consistent with our data. There is no change of the octahedral tilt angle between the δ-WO_3 and ε-WO_3 phases. Instead, the position of the central W atom is shifted in ε-WO_3, which develops a spontaneous polarization along the *a*-axis in the unit cell. Of all WO_3 phases, ε-WO_3 is the only structure, which is noncentrosymmetric. This results in variations of the O–W–O atom distance along the [110] direction, which affect the electrical and optical properties of the ε-phase. In particular, higher E_g for ε-WO_3 relative to δ-WO_3 has been reported.[24]

D. Raman spectroscopy

Figure 5 shows Raman spectra of nano-WO_3 films prepared at different P_{tot}. Peaks 6 and 7 are typical for crystalline WO_3 and are common to several WO_3 phases. These correspond to the symmetric and asymmetric ν(O–W–O) stretching modes.[49,50] Peak 6 has a shoulder at lower wave numbers, which has a maximum at approximately 645 cm^{-1}, characteristic for the monoclinic ε-phase.[50,51] It should be noted that this vibrational band also has been discussed in the literature as being due to hydrated tungsten oxide.[49,52] Our combined RBS, XRD, and Raman spectroscopy data give, however, no evidence of hydrated tungsten oxide, and this can therefore be ruled out. Peaks 2, 4, and 5 correspond to the δ(W–O–W) bending vibrations in monoclinic γ and triclinic δ phases.[51] The intensity of peak 5 can be correlated to the amount of the monoclinc γ-phase according to some reports.[50] The relatively large intensity of peak 5 and the relatively broad peaks 6 and 7 compared to bulk data may also be indicative of the nanoporosity in the films. A relatively high intensity of the band at approximately 330 cm^{-1} is, e.g., reported for $W_{18}O_{49}$ compounds.[53]

Peak 1 agrees with previous reports of the presence of ε-WO_3 phase,[53] consistent with XRD data, but we note that a similar peak has previously also been interpreted as being due to the triclinic δ-phase.[47] However, the presence of a small peak at 184 cm^{-1} (peak 3), which previously has been assigned to the ε phase,[48] supports the interpretation of peak 1 as being due to an ε phase. In spectrum obtained at $P_{tot} = 2.0$ Pa in Fig. 5, the intensity of peak 1 is observed to decrease together with the shoulder at 645 cm^{-1}, compared with spectrum obtained at 1.3 Pa. Simultaneously, the intensity of peak 2 increases, which indicates a higher fraction of the δ or γ phase as P_{tot} increases. In comparison with XRD data in Fig. 3, we see that similar changes occur between $P_{tot} = 1.3$ and 2.0 Pa, where the (002) peak increases. We conclude that a structural transition occurs somewhere between these two values of P_{tot}, where the relative fraction of δ or γ phase increases at the expense of the ε-phase.

A weak vibration at 940 cm^{-1} is observed at 3.3 Pa and 4.0 Pa in Fig. 5, which can be assigned either to the W–O surface mode[54] or a ν(W = O) mode due to terminal

https://doi.org/10.1557/jmr.2012.384 Published online by Cambridge University Press

W = O surface groups, which are reported to be located at about 950 cm^{-1}.[37,52] Since this peak appears on the thinner films, which have higher porosity, it is tempting to attribute it to surface W = O species. It qualitatively correlates with the SEM, RBS, and XRD results above, i.e., the films become more porous with increasing P_{tot}. This is also qualitatively supported by the concomitant increase of the FWHM of peak 6 and 7, which indicates a decrease of the structural order in the films.

E. UV–vis spectroscopy

Absorption in the films was calculated from transmittance and reflectance measurements. Figure 6 shows the absorption coefficient in the wave length range 300–2500 nm for nano-WO_3 films prepared at different P_{tot}. The oscillations, mainly present in the 500–1000 nm wave length range, are interference fringes that are not compensated for by Eq. (7). $T(\lambda)$ is measured at normal incidence and $R(\lambda)$ at a slightly different angle. It is obvious that there is significant absorption in the NIR region, exhibiting a broad peak maximum centered at about 1500 nm, consisting of (at least) two absorption bands. With increasing P_{tot}, the NIR absorption decreases. At P_{tot} = 3.3 and 4.0 Pa, only two weaker NIR bands are observed at 1200 and 1600 nm. The absorption in this range has earlier been attributed to polarons.[55,56] Maxima near 1450 and 1800 nm have previously been observed in a substoichiometric WO_{3-x} ε phase, as reported by Salje.[30] These peaks were ascribed to two types of polarons that occur simultaneously, one extended mobile type and the other more localized.

From the results above, a slightly substoichiometric and strained film structure, which consists of a small amount of the ε phase, is inferred at low P_{tot}. Both the strain and the ε phase gradually disappeared at higher P_{tot}, as evidenced by XRD and Raman spectroscopy. The strength of the polaron absorption indicates that $x \approx 0.01$ at 1.3 Pa and decreases with increasing P_{tot}, in fair agreement with the RBS results. This estimate was obtained from a comparison with published polaron absorption strengths for Li–WO_3 thin films.[57] It is thus evident that optical transmittance and reflectance measurements are much more sensitive to detect small substoichiometries than RBS.

In a simple model, the band gap can be approximated from the slope of the absorptance. We refer to a forthcoming publication for a detailed account of the nature of the interband excitations in WO_3 and the existence of band gap states in nano-WO_3 films. Here, it suffices to note that band gap states contribute significantly to the absorption just below the optical band edge. Figure 7 shows that all absorptance curves meet at ~447 nm or ~2.78 eV. The band-to-band excitations of electrons from the valence band to the conduction band are seen as the steep slope in the short wave length range 300–445 nm. At ~447 nm, the inclination of the slope clearly changes, as marked by the dashed lines in Fig. 7. This marks the demarcation energy, which may be used to approximate the transition between the Urbach tail,[59] and the absorption due to electronic interband transitions. The demarcation energies deduced from the analysis are shown in Table II. The small absorption in the range 448–500 nm is

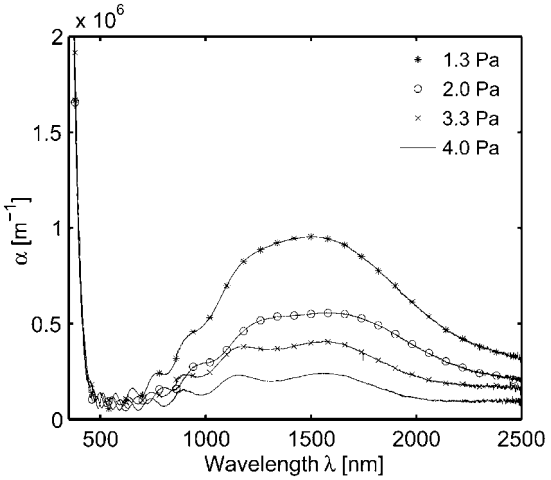


FIG. 6. The absorption coefficient α in the wave length range 300–2500 nm for nano-WO_3 thin films prepared at different P_{tot} between 1.3 and 4.0 Pa.

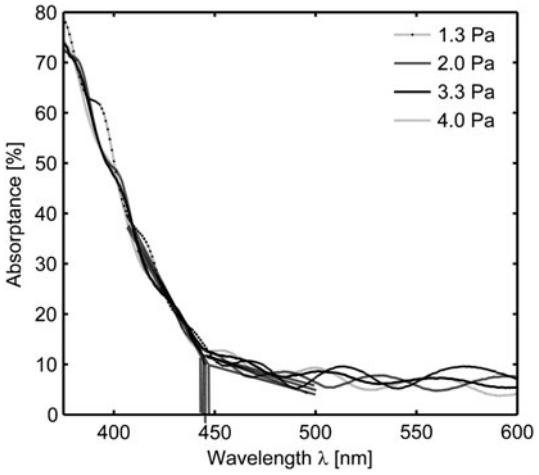


FIG. 7. Absorptance of nano-WO_3 films prepared at different P_{tot} between 1.3 and 4.0 Pa around the optical band edge in the wave length region 300–600 nm.

TABLE II. Band gap energy, E_g, deduced from UV–vis spectrophotometry and crystalline phases derived from XRD and Raman spectroscopy for nano-WO_3 thin films.

Sample	E_g (nm)	E_g (eV)	Phase
a	447	2.77	γ and/or δ, ε
b	448	2.77	γ and/or δ, ε
c	446	2.78	γ and/or δ
d	446	2.78	γ and/or δ

https://doi.org/10.1557/jmr.2012.384 Published online by Cambridge University Press

due to states in the band gap. These states can be caused by the mixing of phases and variations in bond lengths and angles (here evidenced by mixed phases inferred from XRD and Raman spectroscopy data), grain boundaries (here, the grain sizes deduced from XRD are generally smaller than SEM structures, suggesting that the SEM structures contain several grains), or strain effects (here inferred from XRD data and polaron absorption at low P_{tot}). Localized band gap states give rise to a new regime beyond the extended band edges. Photoexcited electrons and holes can interact with these localized states and contribute to photoinduced processes. In Sec. III. F, we explore whether these contribute to photodegradation of SA in comparison with interband excitations across the band edge.

F. Photodegradation of SA

Figure 8 shows the photodegradation of SA as a function of solar light irradiation time in a log-linear plot. It is apparent that the initial decay of the integrated SA absorbance between 2700 and 3000 cm^{-1} as a function of irradiation time obeys first-order kinetics. In comparison with previous work on SA spin coated on TiO_2 using similar procedures, where multilayer SA was inferred,[42] the first-order reaction kinetics indicates that the SA coverage in our case is in the monolayer regime. This is also quantitatively supported by the measured absorbance on the nano-WO_3 films, using the calibrated value for the integrated absorbance unit,[42] and comparing with the estimated number of surface sites from the D35 titration measurements presented above. With these estimates, we obtain a maximum SA coverage of approximately 0.5 monolayer.

From Fig. 8, it is clear that k_{dec} is more than twice as high at P_{tot} = 4.0 Pa compared to 1.3 Pa, under otherwise identical conditions. These observations correlate with the findings above that the low P_{tot} nano-WO_3 films exhibit mixed phase structures, which are associated with strong polaron absorption due to the presence of a substoichiometric and strained film structure. This suggests that even the presence of small amounts of excess electrons in the band gap at approximately 1 eV below conducting band (CB), which give rise to the polaron absorption bands in Fig. 6, effectively can quench photoexcited electron–hole pairs. We propose a possible mechanism that may be responsible for the quenching of photoexcited electron–hole pairs in slightly substoichiometric WO_3. In Fig. 9, we schematically depicted this mechanism. Here, electrons populating localized polaron states rapidly recombine with photoexcited holes. Subsequently, photoexcited CB electrons repopulate these states. This is a relatively fast process compared with the interfacial charge transfer processes of CB electrons to the affinity level on adsorbed O_2. The efficiency of this process depends on the character of the polarons and how extended these states are. The small substoichiometry deduced from the polaron absorption may nevertheless, despite its low value $x \approx 0.01$, affect e–h pair recombination if the spatial extension of the polaron is large. This shows the importance of precise control of the materials synthesis to prepare photoactive WO_3 nanostructures.

Figure 10 shows the PC SA degradation rate, k_{dec}, and the quantum yield, Φ, calculated by means of Eq. (8)

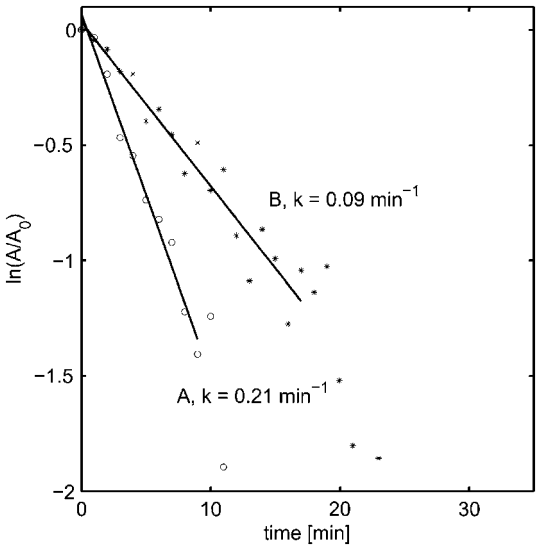


FIG. 8. Semilogarithmic plot of the normalized absorbance due to SA as a function of irradiation time for nano-WO_3 films prepared at different P_{tot}: (A) 4.0 Pa and (B) 1.3 Pa. *A* is the integrated absorbance between 2700 and 3000 cm^{-1} due to the μ(C–H) bands at time, *t*, and A_0 is the absorbance at $t = 0$. Simulated solar light (AM1.5) was used as light source.

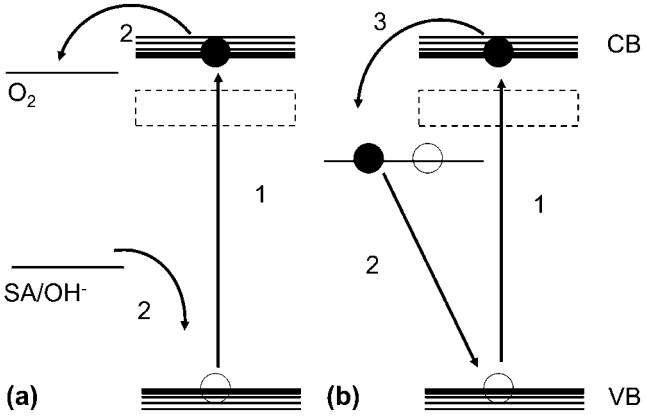


FIG. 9. Schematic pictures of the electronic states in WO_3 responsible for photodegradation of organic molecules in air. (a) Excitation of a VB electron to the CB in stoichiometric WO_3 and interfacial charge transfer (O_2 reduction and organic oxidation) to adsorbed molecules at the surface. (b) Electron–hole pair excitation in substoichiometric WO_{3-x} with localized polaron states ~1 eV below CB gives rise to an electron–hole pair recombination process. The numbers indicate the sequence of reactions. The dashed square represents the location of band gap states responsible for the visible light photoactivity.

https://doi.org/10.1557/jmr.2012.384 Published online by Cambridge University Press

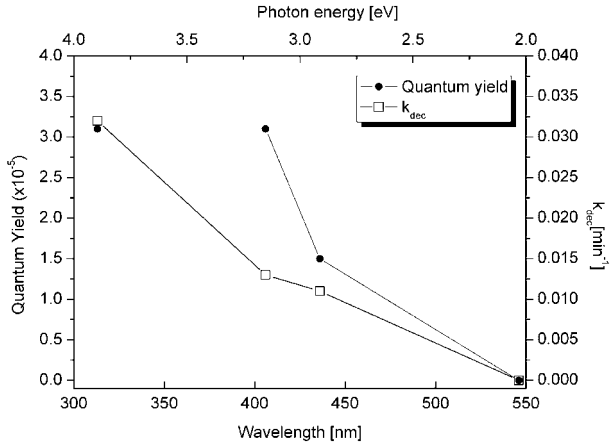


FIG. 10. Quantum yield (left ordinate) and degradation rate k_{dec} (right ordinate) as a function of photon energy (upper abscissa) and wave length (lower abscissa) for a nano-WO_3 film prepared at P_{tot} = 3.3 Pa.

TABLE III. Quantum yield and photodegradation rate of nano-WO_3 film prepared at P_{tot} = 3.3 Pa at different excitation wave lengths.

Wave length (nm)	Photon energy (eV)	Φ ($\times 10^{-5}$)	k_{dec} (min^{-1})
313	3.95	3.1	0.032
406	3.04	3.1	0.013
436	2.84	1.5	0.011
546	2.27	0	0

at different wave lengths for a nano-WO_3 film prepared at P_{tot} = 3.3 Pa. It is seen that k_{dec} decreases continuously up to 436 nm and is zero at 546 nm. Visible light active photodegradation is proved by the nonzero k_{dec} = 0.011 min^{-1} at 436 nm, about one-third of the value at UV photon energies (313 nm).

Table III summarizes the photodegradation data. It is, however, more instructive to look at Φ. The low Φ values compared to measurements in colloidal solutions can be attributed to the inefficient collection of photoexcited electron–hole pairs in the SA/nano-WO_3 film system, where excitations deep in the film must diffuse to the surface of the film to take part in SA photodegradation. Nevertheless, we find that Φ is about 50% lower at 436 nm than at UV energies and is equal at 406 and 313 nm. This suggests that there exists an energy threshold comparable to the demarcation energy estimated from the absorptance data. This gives further support that E_g is around 2.8 eV, in good agreement with previous reports.[60,61] Further, a possible explanation of the lower Φ at 436 nm, may be that the states giving rise to absorption at $h\nu < 2.9$ eV, lie below the affinity level of O_2, so that only hole oxidation occurs at these smaller energies. Hence, in this model, the photooxidation reaction is not truly PC at these low photon energies, a hypothesis that warrants further studies.

IV. CONCLUSION

Nanostructured WO_3 films were prepared using reactive dc magnetron sputtering at different working pressures, P_{tot}. At high P_{tot}, stoichiometric nano-WO_3 films are formed, which exhibit a structure consisting of δ-WO_3, possibly coexisting with γ-WO_3. At low P_{tot}, the nano-WO_{3-x} films are slightly substoichiometric ($|x| < 0.1$), exhibit significant strain, have higher density, and contain significant amounts of the ε-WO_3 phase. These films are also associated with strong polaron absorption. The optical properties of nano-WO_3 films prepared at low and high P_{tot}, respectively, are very different despite their structural similarities and are manifested in their different color and NIR absorption. The energy band gap, defined by the demarcation energy, is, however, similar, $E_g \approx 2.8$ eV (445 nm). The existence of band gap states was inferred from weak absorption in the 450–500 nm region. Comparisons of the photodegradation rate at different P_{tot} showed that photodegradation rate was significantly reduced at low P_{tot}. This is attributed to substoichiometry and existence of a strained ε phase characterized by an efficient recombination process, whereby excess localized electrons in the band gap recombine with photoexcited electron–hole pairs. Wave length-resolved photodegradation measurements of SA showed that the nano-WO_3 films were visible light active up to wave lengths of at least 436 nm. A lower bound for the quantum yield was determined to be approximately 3×10^{-5} for films prepared at high P_{tot} at photon energies larger that the band gap energy. The quantum yield dropped to 50% above the band gap, at 436 nm, which is tentatively attributed to inefficient O_2 reduction due to photon absorption into low lying band gap states.

ACKNOWLEDGMENTS

The authors thank Christian Lejon and Andreas Mattsson for assistance with the PC measurements, Per Petersson with RBS measurements, and Erik Johansson for fruitful discussions. This work was financially supported by Swedish Research Council Grant No. 2010-3514.

REFERENCES

1. M.R. Hoffmann, S.T. Martin, W. Choi, and D.W. Bahnemann: Environmental applications of semiconductor photocatalysis. *Chem. Rev.* **95**, 69 (1995).
2. C.G. Granqvist, A. Azens, P. Heszler, L.B. Kish, and L. Österlund: Nanomaterials for benign indoor environments: Electrochromics for "smart windows", sensors for air quality, and photo-catalysts for air cleaning. *Sol. Energy Mater. Sol. Cells* **91**, 355 (2007).
3. J. Tang, Z. Zou, and J. Ye: Efficient photocatalytic decomposition of organic contaminants over $CaBi_2O_4$ under visible-light irradiation. *Angew. Chem. Int. Ed.* **43**, 4463 (2004).
4. A. Fujishima, X. Zhang, and D.A. Tryk: TiO_2 photocatalysis and related surface phenomena. *Surf. Sci. Rep.* **63**, 515 (2008).

https://doi.org/10.1557/jmr.2012.384 Published online by Cambridge University Press

5. H. Zheng, J.Z. Ou, M.S. Strano, R.B. Kaner, A. Mitchell, and K. Kalantar-Zadeh: Nanostructured tungsten oxide – properties, synthesis, and applications. *Adv. Funct. Mater.* **21**, 2175 (2011).
6. A. Rampaul, I.P. Parkin, S.A. O'Neill, J. DeSouza, A. Mills, and N. Elliott: Titania and tungsten doped titania thin films on glass; active photocatalysts. *Polyhedron* **22**, 35 (2003).
7. X.Z. Li, F.B. Li, C.L. Yang, and W.K. Ge: Photocatalytic activity of WO_x-TiO_2 under visible light irradiation. *J. Photochem. Photobiol., A* **141**, 209 (2001).
8. X. Chen and S.S. Mao: Titanium dioxide nanomaterials: Synthesis, properties, modifications applications. *Chem. Rev.* **107**, 2891 (2007).
9. S.K. Deb: Optical and photoelectric properties and colour centres in thin films of tungsten oxide. *Philos. Mag.* **27**, 801 (1973).
10. C.G. Granqvist: *Handbook of Inorganic Electrochromic Materials* (Elsevier, Amsterdam, 1995).
11. C.G. Granqvist: Electrochromic tungsten oxide films: Review of progress 1993–1998. *Sol. Energy Mater. Sol. Cells*. **60**, 201 (2000).
12. G.B. Smith and C.G. Granqvist: *Green Nanotechnology: Solutions for Sustainability and Energy in the Built Environment* (CRC Press, New York, 2011).
13. J. Zhao and X. Yang: Photocatalytic oxidation for indoor air purification: A literature review. *Build. Environ.* **38**, 645 (2003).
14. H. Shi, X.L. Huang, H. Tian, J. Lv, Z. Li, J. Ye, and Z. Zou: Correlation of crystal structures, electronic structures and photocatalytic properties in W-based oxides. *J. Phys. D: Appl. Phys.* **42**, 1 (2009).
15. H. Wang, P. Xu, and T. Wang: The preparation and properties study of photocatalytic nanocrystalline/nanoporous WO_3 thin films. *Mater. Des.* **23**, 331 (2002).
16. R. Abe, H. Takami, N. Murakami, and B. Ohtani: Pristine simple oxides as visible light driven photocatalysts: Highly efficient decomposition of organic compounds over platinum-loaded tungsten oxide. *J. Am. Chem. Soc.* **130**, 7780 (2008).
17. W.B. Cross, I.P. Parkin, and S.A. O'Neill: Tungsten oxide coatings from the aerosol-assisted chemical vapor deposition of $W(OAr)_6$ (Ar = C_6H_5, C_6H_4F-4, $C_6H_3F_2$-3,4); photocatalytically active γ-WO_3 films. *Chem. Mater.* **15**, 2786 (2003).
18. G. Waldner, A. Bruger, N.S. Gaikwad, and M. Neumann-Spallart: WO_3 thin films for photoelectrochemical purification of water. *Chemosphere* **67**, 779 (2007).
19. W.B. Cross, I.P. Parkin, A.J.P. White, and D.J. Williams: Synthesis and characterisation of tungsten(VI) oxo-salicylate complexes for use in the chemical vapour deposition of self-cleaning films. *Dalton Trans.* 1287 (2005).
20. C. Santato, M. Ulmann, and J. Augustynski: Enhanced visible light conversion efficiency using nanocrystalline WO_3 films. *Adv. Mater.* **13**, 511 (2001).
21. A. Hagfeldt and M. Grätzel: Molecular photovoltaics. *Acc. Chem. Res.* **33**, 269 (2000).
22. C. Howard, V. Luca, and K. Knight: High-temperature phase transitions in tungsten trioxide - the last word? *J. Phys. Condens. Matter* **14**, 377 (2002).
23. Y. Xu, S. Carlson, and R. Norrestam: Single crystal diffraction studies of WO_3 at high pressures and the structure of a high-pressure WO_3 phase. *J. Solid State Chem.* **132**, 123 (1997).
24. P.M. Woodward, A.W. Sleight, and T. Vogt: Ferroelectric tungsten trioxide. *J. Solid State Chem.* **131**, 9 (1997).
25. K.R. Locherer, I.P. Swainson, and E.K.H. Salje: Transition to a new tetragonal phase of WO_3: Crystal structure and distortion parameters. *J. Phys. Condens. Matter* **11**, 4143 (1999).
26. G.A. de Wijs, P.K. de Boer, and R.A. de Groot: Anomalous behavior of the semiconducting gap in WO_3 from first-principle calculations. *Phys. Rev. B* **59**, 2684 (1999).
27. A. Polaczek, M. Pekala, and Z. Obuszko: Magnetic susceptibility and thermoelectric power of tungsten intermediary oxides. *J. Phys. Condens. Matter* **6**, 7909 (1994).
28. A. Aird and E.K.H. Salje: Sheet superconductivity in twin walls: Experimental evidence of WO_{3-x}. *J. Phys. Condens. Matter* **10**, 377 (1998).
29. E.K.H. Salje, S. Rehmann, F. Pobell, D. Morris, K.S. Knight, T. Herrmannsdoerfer, and M.T. Dove: Crystal structure and paramagnetic behaviour of ε-(WO_{3-x}). *J. Phys. Condens. Matter* **9**, 6563 (1997).
30. E.K.H. Salje: Polarons and pipolarons in tungsten oxide, WO_{3-x}. *Eur. J. Solid State Inorg. Chem.* **31**, 805 (1994).
31. D.W. Bullett: A theoretical study of the x-dependence of the conduction band density of states in metallic sodium tungsten bronzes $NaxWO_3$. *Solid State Commun.* **46**, 575 (1983).
32. E. Salje: Structural phase transitions in the system WO_3-$NaWO_3$. *Ferroelectrics* **12**, 215 (1976).
33. A. Hjelm, C.G. Granqvist, and J.M. Wills: Electronic structure and optical properties of WO_3, $LiWO_3$, $NaWO_3$ and HWO_3. *Phys. Rev. B* **54**, 2436 (1996).
34. R. Chatten, A.V. Chadwick, A. Rougier, and P.J.D. Lindan: The oxygen vacancy in crystal phase of WO_3. *J. Phys. Chem. B*. **109**, 3146 (2005).
35. B. Krishnamachari, J. McLean, B. Cooper, and J. Sethna: Gibbs-Thomson formula for small island sizes: Corrections for high vapor densities. *Phys. Rev. B* **54**, 8899 (1996).
36. J. McLean, B. Krishnamachari, and D.R. Peale: Decay of isolated surface features driven by the Gibbs-Thomson effect in an analytic model and a simulation. *Phys. Rev. B* **55**, 1811 (1997).
37. M. Boulova and G. Lucazeau: Crystallite nanosize effect on the structural transitions of WO_3 studied by Raman spectroscopy. *J. Solid State Chem.* **167**, 425 (2002).
38. G.K. Williamson and W.H. Hall: X-ray line broadening from filed aluminium and wolfram. *Acta Metall.* **1**, 22 (1953).
39. A. Roos: Use of an integrating sphere in solar energy research. *Sol. Energy Mater. Sol. Cells* **30**, 77 (1993).
40. R. Swanepoel: Determination thickness optical constants amorphous silicon. *J. Phys. E: Sci. Instrum.* **16**, 1214 (1983).
41. W.Q. Hong: Extraction of extinction coefficient of weak absorbing thin films from spectral absorption. *J. Phys. D: Appl. Phys.* **22**, 1384 (1989).
42. Y. Paz, Z. Luo, L. Rabenberg, and A. Heller: Photooxidative self-cleaning transparent titanium dioxide films on glass. *J. Mater. Res.* **10**, 2842 (1995).
43. A. Mills and M. McFarlane: Current and possible future methods of assessing the activities of photocatalyst films. *Catal. Today* **129**, 22 (2007).
44. D.P. Hagberg, X. Jiang, S. Kaufmann, E. Gabrielsson, M. Linder, T. Marinado, T. Brinck, A. Hagfeldt, and L. Sun: Symmetric and unsymmetric donor functionalization. comparing structural and spectral benefits of chromophores for dye -sensitized solar cells. *J. Mater. Chem.* **19**, 7232 (2009).
45. M. Mayer: M. SIMNRA, A Simulation Program for the Analysis of NRA, RBS and ERDA. *In the 15th International Conference on the Application of Accelerators in Research and Industry*, J.L. Duggan and I.L. Morgan, eds, AIP Conf. Proc. **475**, 541 (1999).
46. P.M. Woodward, A.W. Sleight, and T. Vogt: Structure refinement of triclinic tungsten trioxide. *J. Phys. Chem. Solids* **56**, 1305 (1995).
47. E. Cazzanelli, C. Vinegoni, G. Mariotto, A. Kuzmin, and J. Purans: Low-temperature polymorphism in tungsten trioxide powders and its dependence on mechanical treatments. *J. Solid State Chem.* **143**, 24 (1999).
48. A.G. Souza Filho, J. Mendes Filho, V.N. Freire, A.P. Ayala, J.M. Sasaki, P.T.C. Freire, F.E.A. Melo, J.F. Julião, and U.U. Gomes: Phase transition in WO_3 microcrystals obtained by sintering process. *J. Raman Spectrosc.* **32**, 695 (2001).
49. M.F. Daniel, B. Desbat, B. Gerand, M. Figlarz, and J.C. Lassegues: Infrared and Raman study of WO_3 tungsten trioxides and

https://doi.org/10.1557/jmr.2012.384 Published online by Cambridge University Press

WO_3xH_2O tungsten trioxide hydrates. *J. Solid State Chem.* **67**, 235 (1987).
50. A.G. Souza Filho, P.T.C. Freire, O. Pilla, A.P. Ayala, J. Mendes Filho, F.E.A. Melo, V.N. Freire, and V. Lemos: Pressure effects in the Raman spectrum of WO_3 microcrystals. *Phys. Rev. B* **62**, 3699 (2000).
51. E. Salje: Lattice dynamics of WO_3. *Acta Crystallogr., Sect. A* **31**, 360 (1975).
52. C. Santato, M. Odziemkowski, M. Ulmann, and J. Augustynski: Crystallographically oriented mesoporous WO_3 films: Synthesis, characterization, and applications. *J. Am. Chem. Soc.* **123**, 10639 (2001).
53. S. Hayashi, H. Sugano, H. Arai, and K. Yamamoto: Phase transitions in gas-evaporated WO_3 microcrystals: A Raman study. *J. Phys. Soc. Jpn.* **61**, 916 (1992).
54. A. Kuzmin, J. Purans, E. Cazzanelli, C. Vinegoni, and G. Mariotto: X-ray diffraction, extended x-ray absorption fine structure and Raman spectroscopy studies of WO_3 powders and $(1-x)WO_{3-y}xReO_2$ mixtures. *J. Appl. Phys.* **84**, 5515 (1998).
55. I.G. Augustin and N.F. Mott: Polarons in crystalline and non-crystalline materials. *Adv. Phys.* **50**, 757 (2001).
56. E. Iguchi and H. Miyagi: A study on the stability of polarons in monoclinic WO_3. *J. Phys. Chem. Solids* **54**, 403 (1993).
57. A-L. Larsson, B.E. Sernelius, and G.A. Niklasson: Optical absorption of Li-intercalated polycrystalline tungsten oxide films: Comparison to large polaron theory. *Solid State Ionics* **165**, 35 (2003).
58. F. Wang, C. Di Valentin, and G. Pacchioni: Semiconductor-to-metal transition in WO_{3-x}: Nature of the oxygen vacancy. *Phys. Rev. B* **84**, 073103 (2011).
59. A.S. Ferlauto, G.M. Ferreira, J.M. Pearce, C.R. Wronski, and R.W. Collins: Analytical model for the optical functions of amorphous semiconductors from the near-infrared to ultraviolet: Applications in thin film photovoltaics. *J. Appl. Phys.* **92**, 2424 (2002).
60. D.B. Migas, V.L. Shaposhnikov, V.N. Rodin, and V.E. Borisenko: Tungsten oxides. I. Effects of oxygen vacancies and doping on electronic and optical properties of different phases of WO_3. *J. Appl. Phys.* **108**, 205203 (2010).
61. M. Gillet, K. Aguir, C. Lemire, E. Gillet, and K. Schierbaum: The structure and electrical conductivity of vacuum-annealed WO_3 thin films. *Thin Solid Films* **467**, 239 (2004).

https://doi.org/10.1557/jmr.2012.384 Published online by Cambridge University Press